Elemental dynamics and interactions in a carbonate-buffered, sulfatic and ferruginous lake

D.A.Petrash[1,2], C. Thomazo[3,4], A. Valero[2,5], J.J. Valdés [2], K. Umbría-Salinas[2], T.B. Meador[2,5], V. Chrastný [6], K.O. Konhauser[7]

[1] Czech Geological Survey, 152 00 Prague 5, Czech Republic.

[2] Biology Centre, Czech Academy of Sciences, 37005 České Budějovice, Czech Republic.

[3] UMR CNRS 6282 Biogéosciences, University of Burgundy, Dijon, 21000, France .

[4] Institut Universitaire de France, Paris, 75000, France.

[5] University of South Bohemia, Faculty of Science, 370 05 České Budějovice, Czech Republic/

[6] Czech University of Life Sciences Prague, Czech Republic.

[7] University of Alberta, T6G 2E3 Edmonton AB, Canada.

Corresponding author: Daniel A. Petrash (daniel.petras@geology.cz)

Key Points:

- Lake Medard study offers insight into iron, sulfur, nitrogen cycling in redox-stratified waters
- Seasonal redox shifts affect mineral reactions; carbonate reactions and CO_2 flux alter lake chemistry
- Research aids understanding of microbial-mineral interactions in early Earth's oceans

Abstract

Lake Medard is a recently established post-mining lake in the northwest of Czech Republic that displays significant concentrations of dissolved sulfate (dSO_4^{2-}) and ferrous iron (Fe^{2+}) in its density and redox stratified bottom water column. Siderite-buffered anoxic sediments, also rich in iron(III)-oxyhydroxides, underlie that water column characterized by limited labile organic substrates. This composition sustain a transitional redox state between nitrogenous/ferruginous and euxinic conditions. Our study focuses on the Lake Medard bottom water column elemental concentration profiles, sulfate-sulfur and -oxygen isotope compositions, bioactive ion concentrations, and planktonic microbiome data, combined with mineralogical and isotopic analyses of the upper anoxic sediments. This integrative approach reveals that the internal biogeochemical iron cycling is interlinked with that of nitrogen, sulfur and other redox sensitive metals. Minor seasonal oscillations in the monimolimnion redox potential impact mineral dissolution/(re)precipitation reactions, causing shifts in metal partitioning within anoxic sediments. Carbonate-buffered reactions appear to respond to a subsurface CO_2 flux thereby influencing monimolimnial alkalinity and dissolved inorganic carbon concentrations. These hydrochemical modifications shift the sedimentary redox signals, occasionally favoring carbonate over oxyhydroxide metal-binding processes. Our findings address the fate of newly formed sedimentary oxyhydroxides in a transitional redox-stratified water column featuring ferruginous conditions without quantitative sulfate depletion to provide insights on interlinked biogeochemical processes within a concise framework.

Plain Language Summary

A unique lake formed in an old lignite mining area in the Czech Republic stands out due to high levels of sulfate and iron in its deepest waters. We examined this lake's deep water column and its bottom sediments, analyzing inorganic chemicals, minerals, and microorganisms. Our research reveals that the interlinked iron and sulfur cycling in the lake system are vigorous. Slight environmental changes in the oraganic-substrate depleted bottom water column can significantly impact how iron mineral reactions in the sediments proceed. This study offers insights into similar processes in ancient Earth's oceans, enhancing our understanding of Earth's coupled geological and biological histories.

1 Introduction

A profound understanding of microbe-mineral interactions impacting Precambrian shallow marine facies is necessary for accurately reconstructing Earth's early ocean redox structure and better comprehending the evolution of geosphere-biosphere interactions. Several recent research efforts have focused on investigating the sulfur cycle under ferruginous conditions without a quantitative dSO_4^{2-}depletion (e.g., Mills *et al.*, 2016; Scholz, 2018; van de Velde *et al.*, 2021). However, the transient state enabling such cryptic sulfur cycling to develop is uncommon among the few modern mesotrophic lakes featuring either ferruginous or sulfatic water columns. The former are frequently used as ‘analogues’ for understanding redox stratification in ancient oceans (Koeksoy *et al.*, 2016). Those studies extrapolate, via analogy or actualism, chemical and isotopic observations on modern ferruginous lake systems to interpret geochemical signals preserved in Precambrian open-marine facies (Swanner et al., 2020). Yet, diagenetic models relying on modern low-sulfate lacustrine analogs offer limited insights into Precambrian coastal areas where episodic interactions between ferruginous and sulfate-rich

waters likely occurred due to increased oxidative weathering of terrestrial sulfides. This phenomenon became notably pronounced proceeding the initiation of sulfur redox cycling, especially in coastal marine settings where photosynthetic microbial mats generated micromolar levels of O_2 (e.g., Fakhraee *et al.*, 2019; Dreher *et al.*, 2021; Bayon *et al.*, 2022).

Lake Medard (LM), a recently formed post-mining lake in NW Czech Republic, provides a unique opportunity to examine biogeochemical mechanisms and microbe-mineral interactions in a nitrogenous, ferruginous, and sulfatic bottom water column overlying anoxic ferruginous sediments. The latter contain ferric particles exported from the redoxcline as well Early Miocene siderite redeposited in the lakebed that buffers the water column, maintaining an alkaline to circumneutral pH. Sulfate. On the other hand, is delivered by groundwater recharge (Petrash *et al.*, 2022). Here we relate spectroscopic concentration data of the chemically stratified bottom waters of LM with analyses of the upper anoxic sediments. The solid phases in the sediments were characterized using X-ray diffraction (XRD), Fe_{K1} absorption, and elemental determinations conducted after a mineral-calibrated sequential extraction scheme targeting reactive iron-bearing minerals (Poulton & Canfield, 2005; Claff *et al.*, 2010; Umbría-Salinas *et al.*, 2021). These data were integrated with information on dissolved ions and volatile fatty acid concentrations, $\delta^{34}S$ and $\delta^{18}O$ isotope ratio of dSO_4^{2-}, $\delta^{56}Fe$ values of dissolved (residual) iron (Fe^{2+}), $\delta^{13}C$ and concentration determinations of dissolved inorganic carbon. Additionally, the composition of the planktonic prokaryote community structure, based on amplicon sequence analyses, was considered, along with $\delta^{34}S$ and $\delta^{18}O$ isotope ratios of authigenic gypsum and pyrite, the $\delta^{13}C$ of carbonates present in the claystone-dominated overburden of the former mine pit, and the $\delta^{18}O$ isotope ratios of the bottom lake waters.

This research sheds light on cryptic interlinked elemental cycles relevant to ancient sedimentary systems and elucidates early diagenetic processes in LM sediments currently undergoing alteration beneath a stratified ferruginous and sulfatic water column. We identify complex (bio)hydrogeochemical patterns and trace element cycling that transcends regional importance by shedding light on microbial-mineral interactions pertinent to the evolution of early Earth's oceans. This contribution enriches a broader scientific understanding of biogeochemical cycles, offering an actual perspective on Earth's geosphere and biosphere interplay throughout history

2 Materials and Methods

2.1 Water Sampling and analyses

Samples were collected from the stratified LM bottom water column using a Ruttner sampler at water depths ranging from 47 to 55 m below the surface. Prior to sampling, physicochemical parameters of the water column were measured with a YSI 6600 V2-2 water quality sonde (Xylem Analytics). Based on the probe information, the water column sampling resolution was between 1 and 2 m. This design aimed to achieve a high-resolution understanding of physicochemical properties near the redoxcline at the time of sampling (Fig. 1), approximately 48 ± 1 m, where the redox potential rate of change was higher with respect to depth. The water sample aliquots underwent chromatography, optical and mass spectrometry, sequencing, microscopy, and genomic analyses. Refer to Supporting Information for analytical details.

2.2 Sediment analyses

Replicate sediment cores, collected using an in-house made gravity corer, were analyzed for mineralogy in the upper anoxic sediment column down to 8 cm below the SWI. The cores were subsampled at a 2 cm-resolution in a custom-made glovebox under N-atmosphere, immediately frozen using liquid N_2, and then freeze-dried before sample storage at -18 ºC.

XRD qualitatively assessed sediment mineralogy, while a sequential extraction scheme characterized the partitioning of Fe and Mn, the lanthanide series, and some redox sensitive traces (V, As) into four operationally defined reactive solid phases: (i) Fe carbonates, (ii) easily reducible poorly crystalline Fe(III) oxyhydroxides and manganese(IV) oxides, and (iii) reducible crystalline Fe(III,II) oxyhydroxides (Poulton and Canfield 2005; Claff et al. 2010).

X-ray absorption slightly above the K_1-edge of Fe (7112.1 eV) evaluated the dominant oxidation states of elements in the upper sediment minerals. The samples were stored in an anoxic atmosphere of ≤5 parts per million (ppm) O_2 using a palladium catalyst and H_2 gas mix of 5% (Coy Labs) before analyses at a synchrotron hard X-ray beamline (MicroXAS beamline, SLS-PSI).

Textural analyses of sediments were conducted using Field Emission Scanning Electron Microscopy with Energy Dispersive X-Ray Spectroscopy. Additionally, total organic carbon (TOC) contents were determined, and stable isotope analyses were conducted for $\delta^{34}S$ and $\delta^{18}O$ of gypsum, $\delta^{13}C$ of siderite, and $\delta^{34}S_{CRS}$. For comparison, the $\delta^{13}C$ of siderite, and $\delta^{34}S$ of pyrite present as authigenic phases in the Early Miocene terrigenous were considered. This comparative approach allows determining the stability of isotopic signals upon diagenesis after re-deposition in the modern lake. Refer to Supporting Information for details on sediment preparation, analyses and instrumentation.

3 Study site

Located in the Sokolov mining district, roughly 19 km west-southwest of Karlovy Vary, Czech Republic, the post-mining LM emerged through reclamation of the decommissioned Medard-Libík open-cast lignite mine. Originally formed by infilled water diverted from the nearby Eger (Ohře) river, LM now spans approximately 4.9 km^2 in areal extent, with maximum depths between 48 and 60 meters below the surface at its west and central depocenters, respectively. During the mid-2000s closure and abandonment of the LM mine pit, Fe and sulfate, derived from sedimentary pyrite oxidation, leached into shallow and pit lakes as groundwater filled the topographic post-mining depression (E. Murad et al., 2005; Enver Murad et al., 2003). The hydrochemistry of the resulting shallow pit lakes was further influenced by runoff carrying particles and solutes from weathered Early Miocene tuffaceous and carbonate-rich claystone at the mine overburden. This lithology represents deposition that occurred in an Early Miocene rift lake (Rojík, 2004). Authigenic minerals that accumulated in the shallow pit lakes preceding the present-day, deeper post-reclamation lake included two-line ferrihydrite, schwertmannite, goethite and jarosite; with detrital minerals such as kaolinite and mica also being present (Murad & Rojik, 2003, 2005). The post-reclamation LM is characterized by density, temperature and distinct redox stratification in its bottom water column (Fig 1a). The hydrochemistry of LM is influenced by groundwater-rock interactions, aeolian deposition, and contemporary mineral

transformations of mine spoils and weathered, Early Miocene terrigenous redeposited in the lakebed (Petrash et al., 2022).

4 Results and Discussion

4.1 Dissolved water column species, elemental cycling and upper anoxic sediment reactivity

4.1.1 Water column stratification features minor redox shifts affecting elemental cycling

LM exhibits a stratified water column (Fig. 1a) with a mixolimnion extending from the lake surface to moveable depths approximating 44 to 48 meters. Below the mixolimnion is the distinct hypolimnion transitional zone characterized by gradients in conductivity, salinity, dissolved oxygen (O_2), pH, and temperature (Supporting Information, Table S1). An anoxic monimolimnion lies toward the lakebed (Fig. 1a). This stratified layer is predominantly found in the deepest central and western parts of the lake. In the eastern part, influxes of hypoxic, sulfate-rich groundwater substantially modify the water column's redox structure; possibly resulting from the seasonally absence of the anoxic zone, and with the redoxcline establishing in the sediment below the SWI (Petrash et al., 2022). This intricate redox structure of the newly formed water body was evident in the early water filling stages (Vrzal et al., 2011).

The bottom waters of LM are ferruginous and manganous, with comparable concentrations of dissolved Fe(II) and Mn(II) around 30 μM (Fig. 1b, Table 1) — as determined at the central sampling location (Supporting Information, Fig. S1). In the western depocenter, these metal concentrations may exceed 100 μM (Petrash et al., 2018). Variability in transition metals and sulfate concentrations in LM's bottom water column is attributed to fluid rock interactions with weathered bedrock and/or a differential response to local hydrology, which leads to laterally variable diffuse groundwater recharge from precipitation (Petrash et al., 2022). The Miocene bedrock is argillaceous and contains pyritic coal seams. The embedded lignite exhibits concentrations of lanthanides and arsenic (As) higher than the global average (Bouška et al., 1999).

The solubility of metals governs variations in bottom water column conductivity, abnd are impacted by redox potential fluctuations (Fig. 1a). As sedimentary Fe(III) and manganese (Mn(IV,III) oxyhydroxides of redox-reactive phases with a high affinity for these metals undergo reductive dissolution, dissolved of lanthanides are mobilized from sediments. In consequence, concentrations of these and other redox-sensitive element, such as vanadium, (V), increase diffusively in the water column (Fig. 1c). Figure 1c-d further illustrates the impact of particulate Fe and Mn reactivity on the availability of diffused, bottom water rare earth elements (REE). Mobilization of light REE (LREE) occurs through reductive dissolution. Then upward diffusion across the monimolimnion results in re-complexion of diffused LREE with partially stabilized (i.e., selectively reduced) colloidal Fe(III)-bearing particles exported from the redoxcline, while their heavy counterparts remain in solution. As the diffusive front, relatively enriched in heavy REE (HREE), reaches the dysoxic zone in the hypolimnion, HREE become fully complexed by metastable, poorly crystalline, and highly reactive Fe(III) precipitates. Consequently, their dissolved concentrations rapidly decrease at the redoxcline (Fig 1d). Furthermore, proteins with lanthanophilic properties secreted by homologous microorganisms identified in the microbiome

of LM, such as methylotrophic bacteria, may also play a role (Valdes et al., 2024) thereby warranting further scrutiny regarding relevance and extent.

4.1.2 The carbonate budget

LM's bottom water column exhibits a pH gradient ranging from alkaline to circumneutral (8.2 to 7.4 units), decreasing with increasing depth (Fig. 1a). Simultaneously, dissolved inorganic carbon (DIC) concentrations substantially increase from 1.9 to 9.8 mM (Fig. 2b, Table 1). Alongside this alkalinity increase, DIC's $\delta^{13}C$ values decrease, suggesting the influence the lakebed's ^{13}C-depleted hydrochemical input on the monimolimnial carbon reservoir (Fig. 2b). The dissolution of redeposited Miocene Fe-dolomite and siderite in the modern lakebed can buffer sediment pH while providing substantial carbonate alkalinity to the bottom density stratified waters. On the one hand, dolomite, once abundant in the Miocene "detrital" sediment source to LM, is now < 0.5 wt. % (i.e., the detection limit of semi-quantitative XRD). On the other hand, less soluble siderite accounts for about 4 wt. % of the total mineralogy.

The bulk $\delta^{13}C$ values of LM's anoxic sediments are +6.4 ± 0.3 ‰ (N = 6), primarily from siderite. This contrasts with Miocene carbonate-bearing claystone in the former mine overburden, where siderite has $\delta^{13}C$ values in the range +8.49 to +10.64 ‰ (N=6). In contrast, Miocene dolomite has a broader range of $\delta^{13}C$ values between +1.41 and +7.48 ‰ (N=9). Therefore, the LM's siderite is depleted in ^{13}C by 2 to 4 ‰ compared to the mean $\delta^{13}C$ values of Miocene siderite. Given the observed $\delta^{13}C$ offset of +9.1‰ to +10.9‰ regarding the monimolimnial DIC (Fig. 2b), a small proportion of siderite likely forms on the lakebed, influencing the bulk sediment $\delta^{13}C$ signature towards less positive values. However, the bulk of this carbonate phase is thought to be redeposited and sourced from Miocene strata as determined by using a simple mass balance approach (see below).

To explain the relatively ^{13}C depleted DIC, a source other than dissolution of detrital carbonates must be considered. The DIC in LM bottom waters might be influenced by an active regional influx of geogenic CO_2 with a modal signature $\delta^{13}C$ value between -1.8 and -4.0 ‰ (Geissler, 2005; Weinlich et al., 1999). This geogenic CO_2 flux, migrating through the Eger rift fault systems, has regionally permeated the upper crust and its volcano-sedimentary cover since, at least, the Early Miocene (Mach et al., 2017; Rapprich et al., 2023). Furthermore, a geogenic CO_2 flux can moderately decrease the pH (~0.4 units) of the water column (Fig. 1a.), consistent with the acidifying nature of dissolved CO_2, forming carbonic acid in the lake water, which readily dissociates to release protons thereby lowering the pH while increasing alkalinity (Fig. 2b).

Another potential source of ^{12}C in the monimolimnion is organotrophic respiration, which, depending on dominant metabolic pathways and the type of labile organic matter available, might lead to a moderate decrease in pH (Gallager et al., 2014; Soetaert et al., 2007, Middleburg, 2019). Sedimentary organic matter in LM exhibits a narrow $\delta^{13}C$ range of −27.9 ± 0.1‰ (N = 6). Using this value and the mean $\delta^{13}C$ values in carbonates from the anoxic sediment in a simple linear mixing model (Phillips and Gregg 2001) suggests that about 70 ± 5% of the DIC originates from the dissolution of sedimentary carbonates. The rest is derived from other CO_2 sources, must more likely geogenically dominated given LM's current oligotrophic state. To discern the relative contributions of geogenic sources and organotrophic respiration, it is crucial

to quantify how much DIC can be produced by organotrophic respiration pathways operating within the lakebed and to analyze its stable carbon isotope signature. Efforts towards this end, akin to those detailed in Havas et al., 2023a,b, are currently in progress. Nonetheless, this aspect extends beyond the primary focus of this study and represents an avenue for future research that will build upon our current findings.

4.2 Dissolved sulfate regeneration, consumption and/or solid phase incorporation

Another distinctive feature within the redox and carbonate-buffered LM stratified waters are the relatively high sulfate concentrations, ranging from 5.2 to 17.5 mM, that exhibit a notable increase with depth. A slight decrease in dSO_4^{2-}levels (0.8 mM) approaching the SWI (Fig. 2c) suggests an ongoing sulfate reduction within the monimolimnial waters. Examining the $\delta^{34}S$ values of dSO_4^{2-} concentrations, ranging from +10.9 to +13.4 ‰ (Fig. 2c), statistically significant positive correlation emerges with the $\delta^{34}S$ values of the residual sulfate (Pearson coefficient ≈ 0.970, p-value<0.01). This correlation suggests a direct linear relationship between these two parameters (Table 1). Such an apparent correlation implies differential microbial activity, sulfide reoxidation, and/or discrete sulfur sources with distinct isotopic compositions influence the variability of $\delta^{34}S$ and sulfate concentrations in the stratified LM's water column (Fig. 2c).

A covariation becomes apparent between $\delta^{56}Fe$, of residual Fe, and $\delta^{34}S$, of residual sulfate (cf. Fig. 2a and 2c). The dataset in Table 1 shows a robust correlation between Fe and sulfate concentrations (Pearson coefficient = 0.952, p-value = 0.01) mirroring similar statistical relationships between their isotopic compositions ($\delta^{56}Fe$ and $\delta^{34}S$, Pearson coefficient ≈ 0.947, p-value < 0.05). These findings suggest a closely linked behaviour of dissolved Fe and sulfate in the LM water column. The observed covariation supports precipitation of monosulfide, some serving as precursors for dispersed microcrystalline pyrite (Fig. 3a). Archer & Vance (2006) observed a positive $\delta^{56}Fe$-$\delta^{34}S$ correlation in Late Archean sedimentary pyrite interpreted to reflect simultaneous dissimilatory Fe and sulfur reduction. We confirmed this correlation in our lake sedimments and suggest it mirrors transient sulfatic and ferruginous conditions in the water column during iron snow deposition and alteration, indicating a dynamic interplay in early diagenesis of reactive Fe phases.

Accessory and minor amounts of pyrite and gypsum were also detected in the anoxic sediment (Fig. 3b). The isotopic $^{34/32}S$ composition of gypsum, referred to as $\delta^{34}S_{Gy}$, ranged from -13.9 to -9.6 ‰, which contrasts with the average $\delta^{34}S$ values of dSO_4^{2-} in LM bottom waters (approximately +12.8 ‰; Fig. 2c; Supporting Information, Fig. S2a). This discrepancy indicates that $\delta^{34}S_{Gy}$ recorded a significant fractionation process and that gypsum is not in a redeposited phase as siderite. The apparent fractionation recoreded by gypsum, however, will only operate if the mineral is the direct product of the SO_4^{2-} anions in the LM water column reacting with Ca^{2+} released from the sediments, i.e., from carbonate mineral dissolution. Alternatively, the mineral is not directly precipitated from dSO_4^{2-}in the LM water column, where it remains unsaturated (Table 3), but rather forms from a SO_4^{2-} source that is rather restricted to the sediments. Noteworthy, is that the $\delta^{34}S_{Gy}$ values are relatively closer to those of sedimentary sulfides, (-35.1 < $\delta^{34}S_{CRS}$ < -23.0 ‰; Petrash et al., 2022), implying a common process during authigenesis.

At the SWI, the presence and isotopic signature of pyrite reveal an intricate (hydro)biogeochemical interplay. Pyrite exhibits an isotopic offset of ~38 ‰ (expressed as $^{34}\varepsilon_{CRS\text{-}SO4}$) relative to the mean $\delta^{34}S$ of dissolved SO_4 in the monimolimnion. This offset may indicate isotopic fractionation during incomplete microbial sulfate reduction within an open-system oxidative sulfur cycle (Johnston et al., 2014; Zerkle et al., 2016). Microbial sulfate reduction is limited in this context, as only dispersed amounts of pyrite form. The isotopically enriched Miocene pyrite, exhibiting $\delta^{34}S_{CRS}$ values of between +8 and +27‰ (median 16‰) (Supporting Information 2, Figure S2b), is unlikely a detrital source component for this pyrite, implying the presence of specialized SR bacterial populations capable t drive pyrite precipitation. Their activity, however, has minimal effect on the monimolimnial concentrations of dSO_4^{2-}or Fe^{2+} (Brüchert, 2004; Canfield, 2001). These bacteria could completely oxidize their preferred labile organic substrate and are thus limited by its scarcity—available in nM concentrations or below the quantifiable limit at the LM monimolimnion. These substrates are, in decreasing order of abundance, acetate, formate, pyruvate, and lactate (Petrash et al., 2022).

The solid phase $\delta^{34}S$ values indicate that gypsum in the upper sediment may have incorporated sulfide-derived sulfate. This sulfate moiety in gypsum is ^{18}O-enriched by about 2.0 ± 0.6 ‰, relative to the mean $\delta^{18}O_{SO4}$ of the monimolimnion. This magnitude of enrichment aligns with $\Delta^{18}O_{SO4\text{-}H2O}$ values observed in anaerobically oxidized pyrite products (Balci et al., 2007). Since the $\delta^{18}O$ of the anoxic ambient water ranges between −6.1 and −6.7 ‰, with a mean of -6.5 ‰, then the magnitude of solid phase ^{18}O enrichment in gypsum falls within the expected range when sulfate is partially derived from sulfide oxidized by ferric iron (Böttcher et al., 2001, 2005; Böttcher and Thamdrup, 2001), exemplified by the reaction:

$$3S^0 + 2FeOOH \rightleftharpoons 2FeS + SO_4^{2-} + 2H^+.$$

Consistent with this interpretation, an oxygen isotope effect ($^{18}\varepsilon_{SO4\text{-}amb.\ wat}$) of +9.3 to +10.7 ‰ can be calculated, supporting the notion that S^{-2} oxidation likely involves S-disproportionation (Brunner et al., 2005; Bottrell and Newton 2006). The sulfur and oxygen isotopes near SWI and below sulfate are decoupled, indicating a quantitative cycling within the sediments. Disproportionation involves partial S transition from its oxidized to its reduced state through an intermediate valence state that later disproportionate into sulfate and sulfide. The short-lived, intermediate products (e.g., thiosulfate) rapidly exchange oxygen atoms with water molecules in the anoxic porewater system, before returning to the oxidized dSO_4^{2-}porewater pool. This porewater sulfate reacts with Ca^{2+} solubilized during localized carbonate dissolution, resulting in the observed relative ^{34}S-depleted equant gypsum microcrystals (Fig. 3b). The rapid reaction of sulfide with FeOOH constantly exported from the redoxcline, thus prevents sulfide from substantially accumulating in the sediment, while low levels of dissolved sulfide are maintained in LM bottom waters, e.g., ≤0.3 μM (Petrash et al., 2018, 2022).

4.3 Metal partitioning in the lakebed

Sediment composition and metal partitioning dynamics within the upper anoxic sediments were examined using a suite of X-ray analyses. XRD revealed a sedimentary matrix predominantly composed of kaolinite, mica, and quartz. Embedded within this clayey matrix are minor constituents such as rutile, analcime, siderite and gypsum. The latter minerals each constitute approximately 3-5 wt. %. Pyrite was also present in accessory amounts (≤1 wt. %)

(Fig. 3c). The mineralogy of the present-day LM closely resembles that observed in the Miocene lacustrine facies in the overburden of the former mine (Murad & Rojik, 2003; Kribek et al., 2017)

X-ray absorption near-edge structure (XANES) at the Fe_{K1}-edge indicated the presence of FeOOH polymorphs, notably goethite (Fig. 3d). These polymorphs form organo-mineral aggregates, as observed through scanning electron microscopy of the upper sediment strata (Fig. 4c). The distribution of FeOOH phases in the sediment pile suggests that reductive dissolution diminishes the prevalence of amorphous and poorly crystalline Fe(III) oxide phases delivered from the redoxcline via water column settling but favoring the accumulation of more crystalline forms. Additionally, our δ^{56}Fe isotopic data (illustrated in Fig. 2a) strongly suggest that metastable monosulfide precursors can precipitate near the SWI to later undergo limited stabilization to disperse pyrite, which relative abundance is near the detection limit of the semi-quantitative XRD technique (Fig. 3b-c). On this note, the sedimentary Fe_{py}/Fe_{HR} indicator, as a measure of the extent to which highly reactive iron (Fe_{HR}) is converted to pyrite (Raisw*ell et al*, 2018), was found to be ≤ 0.25. Consistent with the anoxic (ferruginous) character of sediments at the lake floor, the indicator of anoxicity (Fe_{HR}/Fe_T) is > 0.7 (Petrash et al., 2022).

Results of aqueous-mineral equilibrium calculations, shown in Table 3, indicate the potential for certain minerals to precipitate from the overlying water column. These calculations, conducted using the geochemical modeling software PHREEQC, assess the saturation indices of various minerals under two distinct aqueous redox potential regimes observed. In the monimolimnion, peak Eh can oscillate between -210 mV and -80 mV, reflecting the dynamic hydrological state of the stagnant lake is modulated by seasonal precipitation patterns and, subsequently, groundwater recharge. The comparatively higher Eh value of -80 mV is transient, manifesting only after seasonal rainfall events. Nonetheless, the less reductive monimolimnial conditions are ephemeral, with the redox potential near the SWI reverting to a more consistent *ca.* -210 mV due to the diminishing influence of groundwater recharge (Umbria-Salinas et al., 2021).

Most elements are relatively enriched when normalized against standard geochemical baselines (e.g., Wedepohl, 1995) or against concentrations measured in local sedimentary sources to the modern lake system (Supporting Information, Fig. S3). The thermodynamically stable phases (i.e., at chemical equilibrium) in LM's bottom water column (Fig. 4). To evaluate the sedimentary response to the redox shifts detected within the monimolimnion, we implemented a sequential extraction protocol targeting highly reactive Fe-bearing minerals. Our mineral-specific concentration profiling focused on the partitioning of Mn, REE, V, and As (Fig 5-ab, Table 2).

The redox reactivity of Mn is notable, with its aqueous availability and complexation dynamics altered by Eh transitions within the LM water column (Fig. 1b). In addition, Mn plays a prominent role in the transfer of other trace metals, such as REE, from the water column to the SWI and their subsequent uptake by authigenic phases subjected to burial (Tribovillard et al., 2006). Our data suggest that Mn(IV,III) is readily reduced in the water column and subsequently associates in its reduced state with reactive particulate phases (i.e., more stable Fe-oxyhydroxides) that finally reach the lake floor. Under more reductive conditions, this association is evidenced by preferential partitioning into the carbonate fraction, hinting at

decreased export of poorly crystalline, highly reactive phases and diminished complexation capacity of the reducible oxide phases that can effectively exert some Mn(II)-binding. When the redox potential gradient in the bottom water column is less marked, however, Mn(II) complexation with carbonate is readily favoured (Fig. 5a-b, Table 2).

The sediment core profiles further reveal that under the two documented redox potentials, REE exhibit sediment partitioning patterns that compare best with those of Mn. Analysis of positive cerium anomalies points to enrichments of Ce(III) into carbonates under the less reductive conditions (Fig. 5c). Concurrently, negative anomalies indicate solubilization of redox-sensitive Ce(III) bound to easily reducible amorphous oxides, which can in turn be more profusely exported from the redoxcline at times when the water column exhibited more marked Eh gradients. This reflects on mobilization of redox sensitive elements such as cerium at the SWI and below (Fig. 5c). The observed phase distribution patterns emphasize the relative stability of authigenic and sedimentary carbonates for water column-induced changes in REE partitioning, underscoring their importance in the geochemical framework of sedimentary redox-sensitive interpretations (Umbría-Salinas et al., 2021).

In contrast to the other redox-sensitive proxies considered here, V and As exhibit distinctive behaviors in response to the dynamic redox gradients of the water column. At the highest Eh observed, V demonstrates a notable affinity for poorly crystalline oxyhydroxides, an interaction that appears to be intensified at times when an increased proportion of reactive oxyhydroxides, amenable to be partially stabilized in transit to the SWI (Posth *et al.*, 2014), can be more profusely generated at the redoxcline. Evidenced by the depth profiles depicted in Fig. 5a-b, a lower water-column Eh gradient can favour binding of V to crystalline oxyhydroxides. Enrichments of V in the upper sediment layers, associated with crystalline oxyhydroxide, are likely due to changes in mobilization and particulate binding of the vanadate ion $VO_2(OH)_2^{2-}$ under conditions of increased redox potential in the water column. Below a depth of 2 cm, V increasingly associates with carbonates a times when redox potential is decreased (Table 2).

The pattern displayed by As displays contrasts with V, which potentially indicates a more complex set of interactions within the sediment matrix. While As tends to associate with carbonates during marked redox transitions at or near the SWI, (illustrated in Figure 5a-b), in the upper sediment layers, at times when redox buffering by the water column increases, As shifts towards preferential binding with Fe-oxyhydroxides. This behaviour suggests variable interactions with the abundant crystalline Fe(III) phases in the deeper sediment layers, a probable vestige of the geochemical milieu preceding the lake's formation or differential. The reactivity of As in the upper sediment is due to currently unaccounted biogeochemical factors, such as underestimated water column-based microbial As metabolisms (Saunders et al., 2019) or oxidative process driven by electron transfer mechanism involving particle-cell interactions (Valero, Jan & Petrash 2023). Notably, the lower strata of modern lake sediments, rich in jarosite (Murad & Rojik, 2003), exhibited high affinity for As (Karimian et al., 2017). Over time, however, jarosite altered, transitioning to goethite, which now dominates the lakebed geochemical landscape (Figs. 3d and 5e).

4.4 Elemental cycling and microbial community structure at LM

The concentration profiles of dissolved metal at LM reveal a vigorous internal cycling in the water column, impacting recently deposited, highly reactive sediments. This cycling encompasses a sequence of mineralogical transformations influencing the fate of redox sensitive metals and metalloids traversing the redox-stratified water column, alongside colloidal Fe and Mn. Reactive aggregates on the sediment surface serve as a habitat for bacteria colonizing early formed mineral clusters. As these aggregates descend across the stratified water column, the activity of bacterial communities (e.g., Fe- and Mn-reducers and -oxidizers) colonizing the surfaces induce the dissolution and re-precipitation/stabilization of amorphous phases into poorly crystalline phases (Posth et al., 2014). This transformation may progress to partial stabilization into metastable, more crystalline forms, such as lepidocrocite. This latter FeOOH polymorph is found at the SWI, albeit less abundant than goethite (Fig. 3d).

During transit to the SWI, microbial-mineral aggregates interact with various compounds, such as scarcely available organic substrates, humic substances, and planktonic prokaryotes. Some of these prokaryotes may be capable of transferring electron to and from the conductive Fe(II, III)-bearing particles (see Valero et al., 2024). Reflecting other systems in the past, LM represents a dynamic ecosystem where microbial interactions in the water column play a central role in the cycling not only of Fe, S and C but also other interlinked elements (Posth et al., 2014).

Genomic analyses (ENA accession: PRJEB47217) underscore the prevalence of δ- and β-proteobacterial groups in the LM microbial community. In the upper hypolimnion, members of the *Gallionellaceae* family are integral to an Fe-oxidizing-nitrate-reducing community inducing metastable Fe(III) precipitation. These precipitates descend and partially dissolve in the monimolimnion due to the activity of Fe reducers like *Geobacter* spp., releasing metals complexed to the aggregates back in the solution. Despite sulfate reducers near the SWI, microbial activity remains restrained owing to a general lack of labile organic substrates. This significantly restricts sulfide production until relative formate enrichment, as demonstrated by Valero et al. (2024), which stimulates their activity, results in precursory pyrite formation. Recent experiments also show that in LM's anoxic waters, distinct Gallionellaceae may engage in a extracellular electron transfer, impacting sulfur, Fe, and nitrogen cycling with the involvement of other EET-capable microbes, for example *Desulfobulbaceae*. This interaction appears crucial for stabilizing Fe(III) minerals and influencing As complexation (Valero et al., 2023).

5 Summary and Conclusions

We utilized spectroscopic methods to analyze the gradients of dissolved C, N, S, Fe, and Mn in the redox-stratified LM, revealing it features a unique intermediate state between nitrogenous and euxinic conditions. This state results from active sulfur and iron co-recycling, influenced by the reducible Fe and Mn proportions avaaible at the from anoxic sediments. Analyzing the interplay of microbial dynamics, mineral transformations, and redox-sensitive geochemical cycles in the post-mining LM offers a novel perspective on the complex interactions shaping the evolution of early biosphere-geosphere interactions.Through this research, we present a comprehensive model bridging the gap between modern analogs and ancient marine settings, emphasizing the dynamic nature of geochemical processes and their enduring impact on Earth's history.

Outlined below are key observations and interpretations governing the geochemical and geomicrobiological processes within the LM redox-stratified water column. Additionally, we highlight their consequential impact on elemental cycling and mineral partitioning in the stratified water column and its underlying anoxic sediments.

1. The density and salinity-stratified water column of LM exhibits redox gradients, particularly across the anoxic monimolimnion. In the upper anoxic sediments, the redox-sensitive metals content bound to minerals subjected to reductive dissolution substantially shift due to mobilization from seasonal redox potential changes in the monimolimnion.

2. The $^{\delta 56}$Fe proxy validates a water-column centered Fe cycling dynamics, corroborating reductive dissolution and re-precipitation processes that affect metal solubility within the LM bottom water column and the SWI. Sulfate reduction and potential monosulfide precipitation occurs near the SWI. As supported by $^{\delta 34}$S, δ^{18}O data, re-oxidization of most sulfide potentially involves S disproportionation. These lakebed processes result in ^{34}S-depleted gypsum compared to dSO_4^{2-} in the monimolimnion, yet it reflects the $^{\delta 18}$O signature of the ambient anoxic water. This phenomenon points to a mixed source sulfate, although dominated by sulfate sourced from the bedrock.

3. Redeposited Miocene carbonates, particularly siderite, buffer the LM bottom water pH, while an active regional influx of geogenic DIC flux influences dissolved carbonate ion budgets and carbonate co-precipitation potential at the lakebed. Spectrometry from XRD and XANES reveal minor changes in redox potential of the bottom waters resulting in variations in the production and export of newly formed amorphous and metastable oxyhydroxides at the redoxcline to the sediments.

4. Dominance of proteobacterial groups and identified microbial communities highlight their pivotal role in metal respiration, electron transfer mechanisms, and biogeochemical cycling of Fe, S, and C among other interlinked elements. Distinct *Gallionellaceae* species, and similar syntrophic microbes capable of engaging in EET from Fe(III)-phases, are potentially integral in such interactions that lead to Fe(III) mineral stabilization within anoxic sediments and mediating metal cycling within the redox stratified water column.

5. Reductive dissolution, re-complexation, and co-precipitation are primary processes governing the solubility dynamics of metals, such as Fe, Mn, V, As, and REE, within the LM water column and the underlying highly reactive, redox- (ferrous Fe) and carbonate-buffered anoxic sediments. Incorporating observations on bottom water column redox fluctuations provides a nuanced perspective on fluid-rock/mineral interactions and biogeochemical cycling in stratified aquatic systems.

6. Redox fluctuations, particularly Fe speciation, significantly influence the behavior of reactive solutes through Fe redox cycling that are intricately linked with the cycling of nitrogen, sulfur, and other redox-sensitive metals. Minor seasonal changes in the bottom water column redox potential can significantly impact interactions involving mineral dissolution and (re)precipitation reactions, as well as the metabolic functioning of the lake. Furthermore, subtle shifts in the redox state of the bottom water column can induce transients in metal partitioning within anoxic sediments, influenced by carbonate-buffered reactions driven by

subsurface CO_2 flux, altering monimolimnial alkalinity and dissolved inorganic carbon levels.

Acknowledgments

The authors have no conflict of interest to declare. Our sincere thanks go to Stefan Lalonde (Université de Bretagne Occidentale) for conducting the iron isotopes analyses, contributing significantly to the depth and scope of this research. We thank Dario Ferreira Sanchez for technical support during beamline experiments at MicroXAS (SLS-PSI, #20161155)

Open Research

All data that support the findings of this study are available in Tables 1- 3 of this article, and in the Supporting Information. In addtion, the datasets for this research have been available in Zenodo: DOI [will be included during revision round, and before publication, essentially all data presented in Tables 1 to 3 and SI, contained in a single excel file].

ORCID Daniel Petrash: 0000-0001-5039-0543

References

Archer C, Vance D (2006) Coupled Fe and S isotope evidence for Archean microbial Fe(III) and sulfate reduction. Geology 34, 153–156.

Balci N, Shanks WC, Mayer B, Mandernack KW (2007) Oxygen and sulfur isotope systematics of sulfate produced by bacterial and abiotic oxidation of pyrite, *Geochimica et Cosmochimica Acta*, 71, 3796–3811.

Bayon, G., Bindeman, I. N., Trinquier, A., Retallack, G. J., & Bekker, A. (2022). Long-term evolution of terrestrial weathering and its link to Earth's oxygenation. *Earth and Planetary Science Letters, 584*, 117490. doi: 10.1016/J.EPSL.2022.117490

Bouška, V., & Pešek, J. (1999). Quality parameters of lignite of the North Bohemian Basin in the Czech Republic in comparison with the world average lignite. *International Journal of Coal Geology*, *40*(2–3), 211–235. doi: 10.1016/S0166-5162(98)00070-6

Brüchert, V. (2004). Physiological and ecological aspects of sulfur isotope fractionation during bacterial sulfate reduction. *Special Paper of the Geological Society of America*, *379*, 1–16. doi: 10.1130/0-8137-2379-5.1

Busigny, V., Planavsky, N. J., Jézéquel, D., Crowe, S., Louvat, P., Moureau, J., Viollier, E., & Lyons, T. W. (2014). Iron isotopes in an Archean ocean analogue. *Geochimica et Cosmochimica Acta*, *133*, 443–462. doi: 10.1016/j.gca.2014.03.004

Canfield, D. E. (2001). Biogeochemistry of Sulfur Isotopes. *Reviews in Mineralogy and Geochemistry*, *43*(1), 607–636. doi: 10.2138/GSRMG.43.1.607

Claff, S. R., Sullivan, L. A., Burton, E. D., & Bush, R. T. (2010). A sequential extraction procedure for acid sulfate soils: Partitioning of iron. *Geoderma*, *155*(3–4), 224–230. doi: 10.1016/J.GEODERMA.2009.12.002

515 Dreher, C. L., Schad, M., Robbins, L. J., Konhauser, K. O., Kappler, A., & Joshi, P. (2021).
516 Microbial processes during deposition and diagenesis of Banded Iron Formations. *PalZ*
517 *2021 95:4*, *95*(4), 593–610. doi: 10.1007/S12542-021-00598-Z

518 Fakhraee, M., Hancisse, O., Canfield, D. E., Crowe, S. A., & Katsev, S. (2019). Proterozoic
519 seawater sulfate scarcity and the evolution of ocean–atmosphere chemistry. *Nature*
520 *Geoscience 2019 12:5*, *12*(5), 375–380. doi: 10.1038/s41561-019-0351-5

521 Geissler, W. H. (2005). *Scientific Technical Report STR05/06:Seismic and Petrological*
522 *Investigations of the Lithosphere in the Swarm-Earthquake and CO Degassing Region*
523 *Vogtland/NW-Bohemia in der Helmholtz-Gemeinschaft*. Potsdam. doi: 10.2312/GFZ.b103-
524 05063

525 Johnston, D. T., Gill, B. C., Masterson, A., Beirne, E., Casciotti, K. L., Knapp, A. N., &
526 Berelson, W. (2014). Placing an upper limit on cryptic marine sulphur cycling. *Nature*,
527 *513*(7519), 530–533. doi: 10.1038/nature13698

528 Karimian, N., Johnston, S. G., & Burton, E. D. (2017). Antimony and Arsenic Behavior during
529 Fe(II)-Induced Transformation of Jarosite. *Environmental Science and Technology*, *51*(8),
530 4259–4268. doi: 10.1021/ACS.EST.6B05335/SUPPL_FILE/ES6B05335_SI_001.PDF

531 Koeksoy, E., Halama, M., Konhauser, K. O., & Kappler, A. (2015). *Using modern ferruginous*
532 *habitats to interpret Precambrian banded iron formation deposition*. doi:
533 10.1017/S1473550415000373

534 Mach, K., Žák, K., Teodoridis, V., & Kvaček, Z. (2017). Consequences of Lower Miocene CO2
535 degassing on geological and paleoenvironmental settings of the Ahníkov/Merkur Mine
536 paleontological locality (Most Basin, Czech Republic). *Neues Jahrbuch Für Geologie Und*
537 *Paläontologie - Abhandlungen*, *285*(3), 235–266. doi: 10.1127/NJGPA/2017/0680

538 Mills, J. V., Antler, G., & Turchyn, A. V. (2016). Geochemical evidence for cryptic sulfur
539 cycling in salt marsh sediments. *Earth and Planetary Science Letters*, *453*, 23–32. doi:
540 10.1016/J.EPSL.2016.08.001

541 Murad, E., & Rojík, P. (2005). Iron mineralogy of mine-drainage precipitates as environmental
542 indicators: review of current concepts and a case study from the Sokolov Basin, Czech
543 Republic. *Clay Minerals*, *40*(4), 427–440. doi: 10.1180/0009855054040181

544 Murad, Enver, & Rojík, P. (2003). Iron-rich precipitates in a mine drainage environment:
545 Influence of pH on mineralogy. *American Mineralogist*, *88*(11-12 PART 2), 1915–1918.
546 doi: 10.2138/am-2003-11-1234

547 Petrash, D. A., Jan, J., Sirová, D., Osafo, N. O.-A., & Borovec, J. (2018). Iron and nitrogen
548 cycling, bacterioplankton community composition and mineral transformations involving
549 phosphorus stabilisation in the ferruginous hypolimnion of a post-mining lake.
550 *Environmental Science. Processes & Impacts*, *20*(10), 1414–1426. doi:
551 10.1039/c8em00328a

552 Petrash, D. A., Steenbergen, I. M., Valero, A., Meador, T. B., Paces, T., & Thomazo, C. (2022).
553 Aqueous system-level processes and prokaryote assemblages in the ferruginous and sulfate-
554 rich bottom waters of a post-mining lake. *Biogeosciences*, *19*(6), 1723–1751. doi:
555 10.5194/bg-19-1723-2022

Phillips, D. L. and Gregg, J. W. (2001). Uncertainty in source partitioning using stable isotopes. *Oecologia*, *127*, 171–179.

Posth, N. R., Canfield, D. E., & Kappler, A. (2014). Biogenic Fe(III) minerals: From formation to diagenesis and preservation in the rock record. *Earth-Science Reviews*, *135*, 103–121. doi: 10.1016/j.earscirev.2014.03.012

Poulton, S. W., & Canfield, D. E. (2005). Development of a sequential extraction procedure for iron: implications for iron partitioning in continentally derived particulates. *Chemical Geology*, *214*(3–4), 209–221. doi: 10.1016/J.CHEMGEO.2004.09.003

Raiswell, R., Hardisty, D. S., Lyons, T. W., Canfield, D. E., Owens, J. D., Planavsky, N. J., Poulton, S. W., & Reinhard, C. T. (2018). The iron paleoredox proxies: A guide to the pitfalls, problems and proper practice. *American Journal of Science*, *318*(5), 491–526. doi: 10.2475/05.2018.03

Rapprich, V., Čáp, P., Erban Kochergina, Y. V., Kadlecová, E., Benkó, Z., Sakala, J., Rodovská, Z., Matějů, J., & Petrash, D. A. (2023). Interactions between distal epiclastic and bio-chemogenic sedimentation at the foothills of a mafic alkaline volcano: The case of the Oligocene Doupovské Hory Volcanic Complex (Czech Republic). *Depositional Record*, *9*(4), 871–894. doi: 10.1002/dep2.240

Rojík, P. (2004). New stratigraphic subdivision of the Tertiary in the Sokolov Basin in Northwestern Bohemia. *Journal of the Czech Geological Society*, *49*(3–4), 173–185.

Saunders, J. K., Fuchsman, C. A., McKay, C., & Rocap, G. (2019). Complete arsenic-based respiratory cycle in the marine microbial communities of pelagic oxygen-deficient zones. *Proceedings of the National Academy of Sciences of the United States of America*, *116*(20), 9925–9930. doi: 10.1073/PNAS.1818349116/SUPPL_FILE/PNAS.1818349116.SAPP.PDF

Scholz, F. (2018). Identifying oxygen minimum zone-type biogeochemical cycling in Earth history using inorganic geochemical proxies. *Earth-Science Reviews*, *184*(August), 29–45. doi: 10.1016/j.earscirev.2018.08.002

Swanner, E. D., Lambrecht, N., Wittkop, C., Harding, C., Katsev, S., Torgeson, J., & Poulton, S. W. (2020). The biogeochemistry of ferruginous lakes and past ferruginous oceans. *Earth-Science Reviews*, 103430. doi: 10.1016/j.earscirev.2020.103430

Umbría-Salinas, K., Valero, A., Jan, J., Borovec, J., Chrastný, V., & Petrash, D. A. (2021). Redox-driven geochemical partitioning of metal(loid)s in the iron-rich anoxic sediments of a recently flooded lignite mine pit: Lake Medard, NW Czechia. *Journal of Hazardous Materials Advances*, *3*, 100009. doi: 10.1016/j.hazadv.2021.100009

Valero, A., Jan, J., & Petrash, D. (2023). Anaerobic dissolved As(III) removal from metal-polluted waters by cathode-stabilized Fe(III)-oxyhydroxides. *Environmental Science: Water Research & Technology*. doi: 10.1039/D2EW00844K

van de Velde, S. J., Reinhard, C. T., Ridgwell, A., & Meysman, F. J. R. (2021). Bistability in the redox chemistry of sediments and oceans. *Proceedings of the National Academy of Sciences of the United States of America*, *117*(52), 33043–33050. doi: 10.1073/PNAS.2008235117

Weinlich, F. H., Bräuer, K., Kämpf, H., Strauch, G., Tesař, J., & Weise, S. M. (1999). An active subcontinental mantle volatile system in the western Eger rift, Central Europe: Gas flux,

isotopic (He, C, and N) and compositional fingerprints. *Geochimica et Cosmochimica Acta*, *63*(21), 3653–3671. doi: 10.1016/S0016-7037(99)00187-8

Zerkle, A. L., Jones, D. S., Farquhar, J., & Macalady, J. L. (2016). Sulfur isotope values in the sulfidic Frasassi cave system, central Italy: A case study of a chemolithotrophic S-based ecosystem. *Geochimica et Cosmochimica Acta*, *173*, 373–386. doi: 10.1016/J.GCA.2015.10.028

Figure 1. Redox-driven solubility and mobility patterns in LM's bottom water column: (a). Redox potential, pH and conductivity variations with increasing water column depths. (b). Profiles of dissolved Fe and Mn concentrations. (c-d). Increasing trends in dissolved, As, V, and REE concentrations are likely regulated by the reductive dissolution of Fe(III) and Mn(IV,III) oxyhydroxides sinks, occurring diffusively from sedimentary sources (and water column sinks). (d). The reductive dissolution of phases with a high affinity for light REEs (LREEs) in sediments, and their subsequent re-complexation with Fe(III)-bearing colloids in solution allow for the persistence of heavy REEs (HREEs) until their precipitative removal in the dysoxic hypolimnion (at above 49 m depth).

Figure 2. Geochemical gradients in LM's stratified water column: (a). Fe concentration profiles and δ^{56}Fe isotopic values. (b). Dissolved inorganic carbon (DIC) concentrations alongside δ^{13}C values. (c). Sulfate concentrations with δ^{34}S values of dSO_4^{2-}.

Figure 3. Mineralogical Analyses Part 1: (a-b). Microscopic features of S-bearing mineral in LM sediments, captured using scanning electron microscopy (SEM). Panel (a) showcases equant gypsum microcrystals and panel (b) exhibits an accessory pyrite microcrystal. (c). Semi-quantitative results derived from X-ray diffraction (XRD). The Rietveld refinement method was employed to enhance the precision of phase identification and quantification, providing insights into the mineralogical composition of the analyzed samples (d). X-ray Absorption Near-Edge Structure (XANES) of bulk sediments: The inset highlights the spectral characteristics at the pre-edge region. The spectrum is predominantly characterized (90 ± 4% fit) by two components in an octahedral coordination environment: goethite > lepidocrocite, which together account for 74–79% of the total variance in the Fe-bearing phases. An additional 26–21% is attributable to Fe(II)-bearing, mixed-valence hercynite ($Fe^{2+,3+}Al_2O_4$) clay as a third significant component.

Figure 4. Eh-pH (Pourbaix) diagram depicting the behavior of Fe (a) and sulfate (b) species below the redoxcline in LM. This diagram goes beyond Eh and pH, incorporating temperature and major element concentrations as influencing factors (for details, see Table 1). With increasing Eh at greater depths, the arrangement of points reflects a depth-dependent perspective, elucidating potential shifts in equilibrium phases within the dynamic hydrochemistry of LM. Crosses on the diagram indicate samples taken at maximal Eh ranges, while dots represent water column measurements when the monimolimnion Eh was at more prevalent -210 mV.

Figure 5. Mineralogical analyses. Part 2: (a). Concentrations of Fe (wt%), and Mn, V, As, and the sum of lanthanides (mg kg^{-1}) in sediment samples, determined post sequential extraction and spectroscopic analysis of extracts. (b). Proportional distribution of metal(loid) fractions in the reactive Fe phases considered, determined as a fraction of total Fe. (c). Application of REE

systematics to cerium-lanthanum anomalies, highlighting the pronounced variation in anomalies within reactive Fe(III)-oxyhydroxide phases compared to more consistent trends in carbonates influenced by the same redox buffering effect of the overlying ferruginous and sulfatic water column. (d). Scanning electron microscopy (SEM) images illustrating FeOOH aggregate abundance and texture in the upper anoxic LM's sediments. Other phases often observed are kaolinite, K-feldspar, muscovite and detrital siderite (arrow) (e): backscattered SEM detail of the analytical area shown in "(d)" showing an organo-mineral FeOOH aggregate.

Table 1. Dissolved concentrations of manganese (Mn^{2+}) and dissolved concentrations and stable isotope ratios of iron (Fe^{2+}), inorganic carbon (i.e., $\Sigma CO_2 = H_2CO_3 + HCO_3^- + CO_3^{2-}$) and sulfate ($SO_4^{2-}$) at the central deepest part of LM (47 to 55 m depth below the surface). The corresponding physicochemical parameters and dissolved trace metal contents pertaining the sampled bottom water column are shown in the Supporting Information, Table S1

Table 2. Concentrations of Al, Fe (wt%), and Mn, V, As, the sum of lanthanides, and redox sensitive Ce (mg kg^{-1}), along with Ce anomalies (Ce*) in LM's anoxic sediment cores from 0 to 8 cm depth. These concentrations were determined after sequential extraction and spectroscopic analysis of the extracts. Sediment samples were collected under varying Eh conditions in the overlying bottom water column, specifically from monimolimnion layers at -180 and -90 mV. TOC values, exhibiting minor variability, are further detailed in the footnote of this table.

Table 3. Saturation indices (log (IAP/K_{sp})) estimated for various minerals in theoretical equilibrium with LM's bottom water column at two distinct peak mean monimolimnial's redox potentials (i.e., -210 and -80 mV).

Figure 1.

(a)

pH

7.7 7.8 7.9 8.0 8.1

O_2 > 253 (µM)

Conductivity (µS cm^{-1})

2000 4000 6000

4.4 °C

8.6 °C

O_2 < 0.9 (µM)

depth (m)

47 48 49 50 51 52 53 54 55

SWI

SWI

-200 -100 0 100

Eh (mV)

(b)

Fe (µM) Mn (µM)

0 10 20 30 40

SWI

(c)

As (nM)

0 100 200 300

ΣLREE (nM)

0 200 400 600

depth (m)

47 48 49 50 51 52 53 54 55

SWI

SWI

0 2 4 6

V (nM)

0 20 40 60

ΣHREE (nM)

(d)

HREE/LREE

0 0.1 0.2 0.3

SWI

Figure 2.

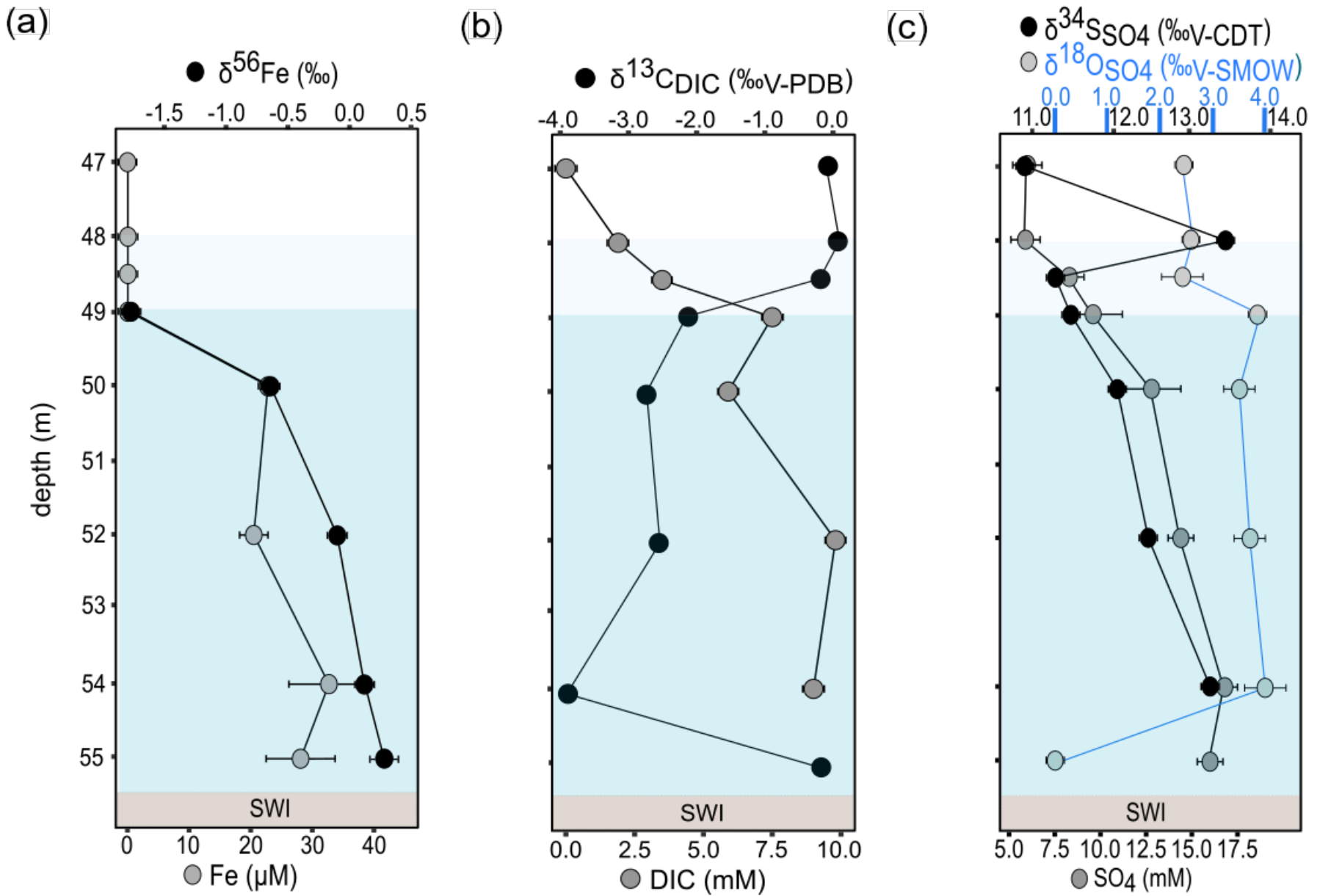
(a)
δ56Fe (‰)
-1.5 -1.0 -0.5 0.0 0.5
depth (m)
47 48 49 50 51 52 53 54 55
SWI
0 10 20 30 40
Fe (μM)
(b)
δ13CDIC (‰V-PDB)
-4.0 -3.0 -2.0 -1.0 0.0
SWI
0.0 2.5 5.0 7.5 10.0
DIC (mM)
(c)
δ34SSO4 (‰V-CDT)
δ18OSO4 (‰V-SMOW)
0.0 1.0 2.0 3.0 4.0
11.0 12.0 13.0 14.0
SWI
5.0 7.5 10.0 12.5 15.0 17.5
SO4 (mM)

Figure 3.

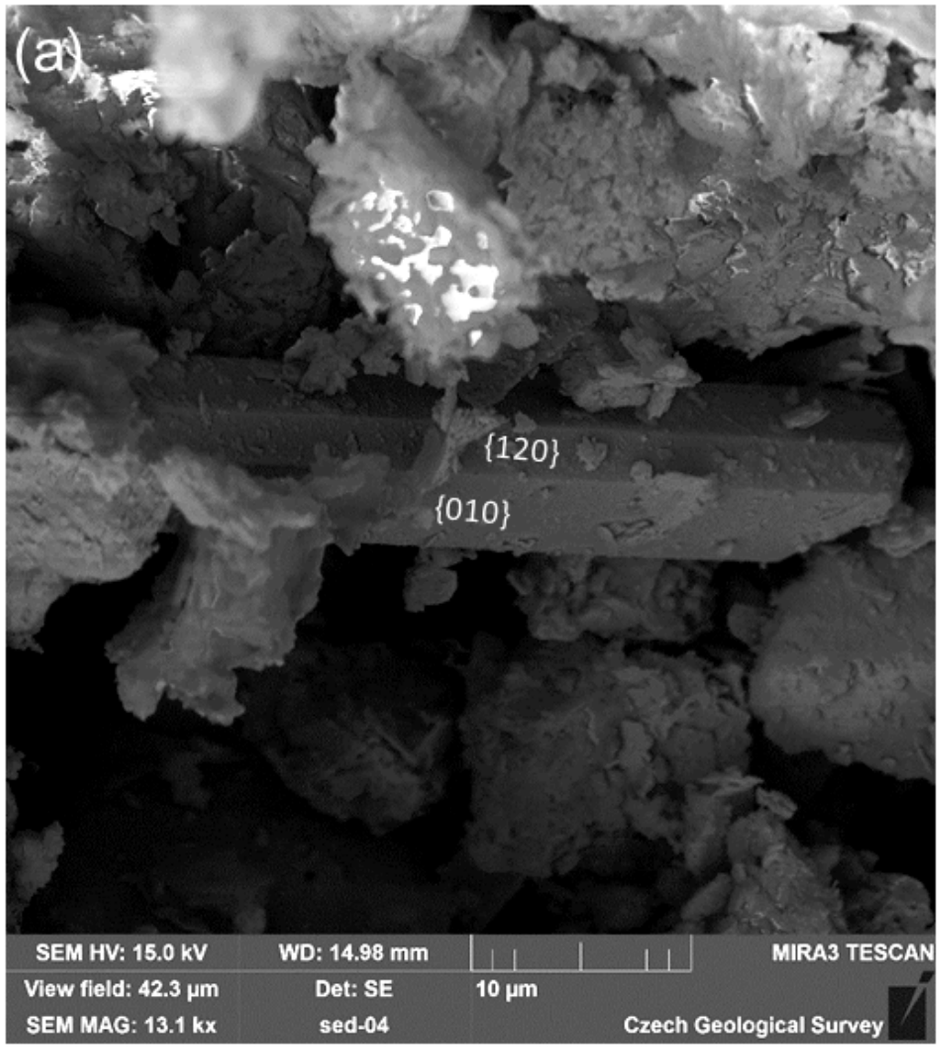
(a)
{120}
{010}
SEM HV: 15.0 kV
WD: 14.98 mm
MIRA3 TESCAN
View field: 42.3 µm
Det: SE
10 µm
SEM MAG: 13.1 kx
sed-04
Czech Geological Survey

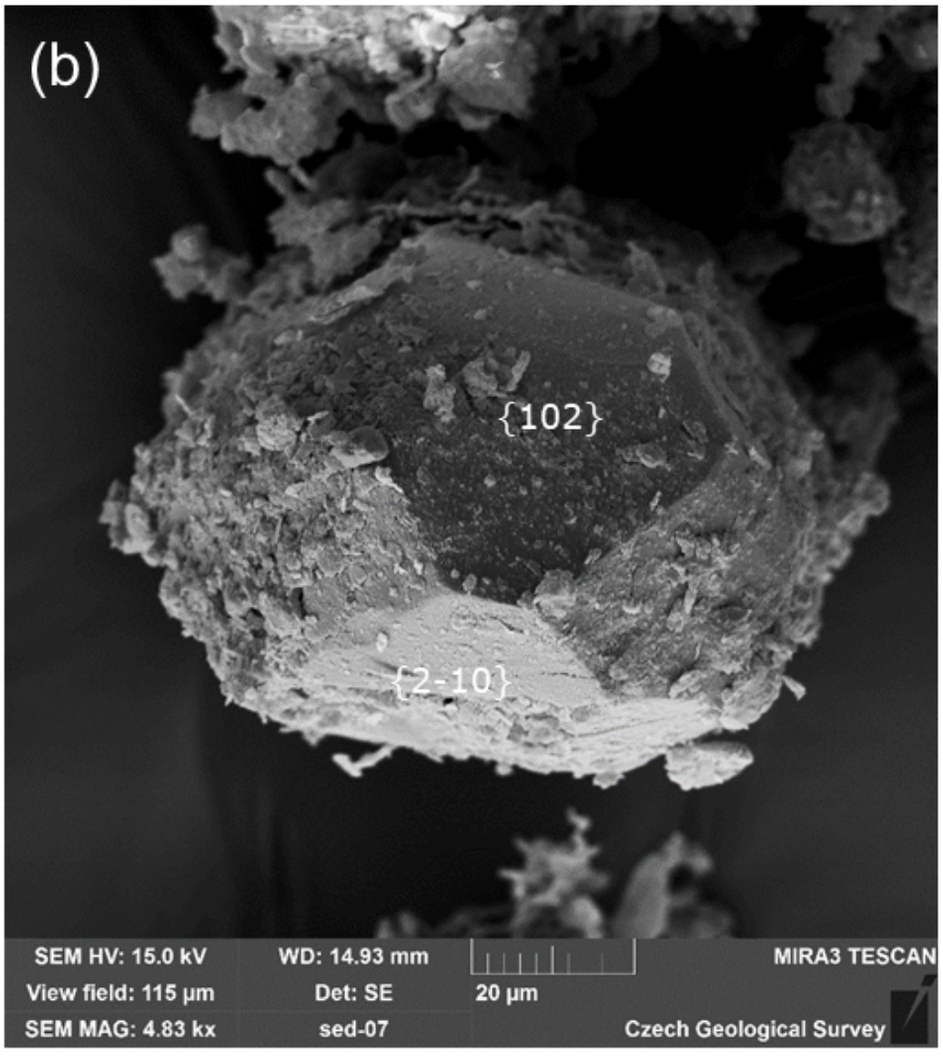
(b)
{102}
{2-10}
SEM HV: 15.0 kV
WD: 14.93 mm
MIRA3 TESCAN
View field: 115 µm
Det: SE
20 µm
SEM MAG: 4.83 kx
sed-07
Czech Geological Survey

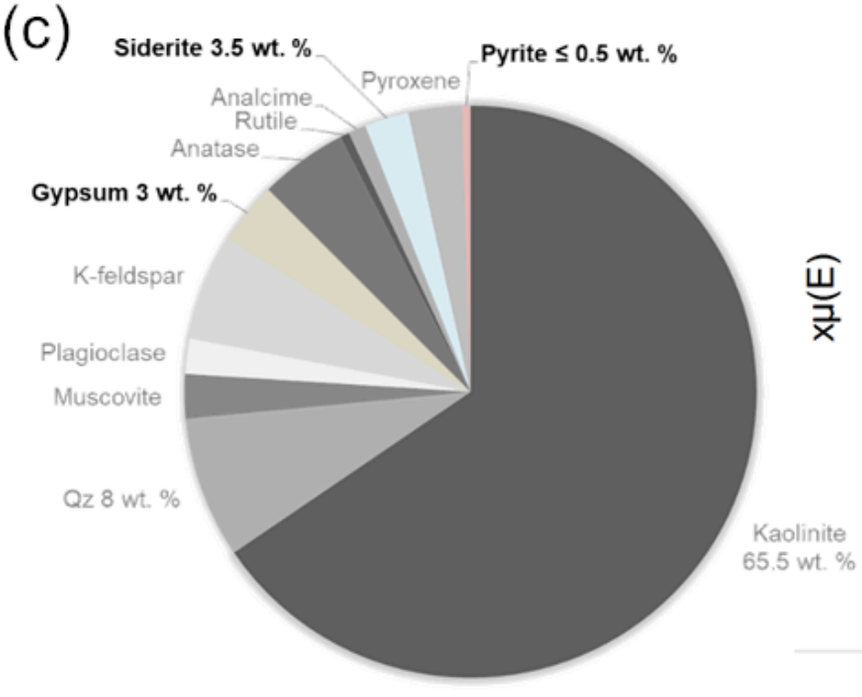
(c)
Siderite 3.5 wt. %
Pyrite ≤ 0.5 wt. %
Pyroxene
Analcime
Rutile
Anatase
Gypsum 3 wt. %
K-feldspar
Plagioclase
Muscovite
Qz 8 wt. %
Kaolinite
65.5 wt. %

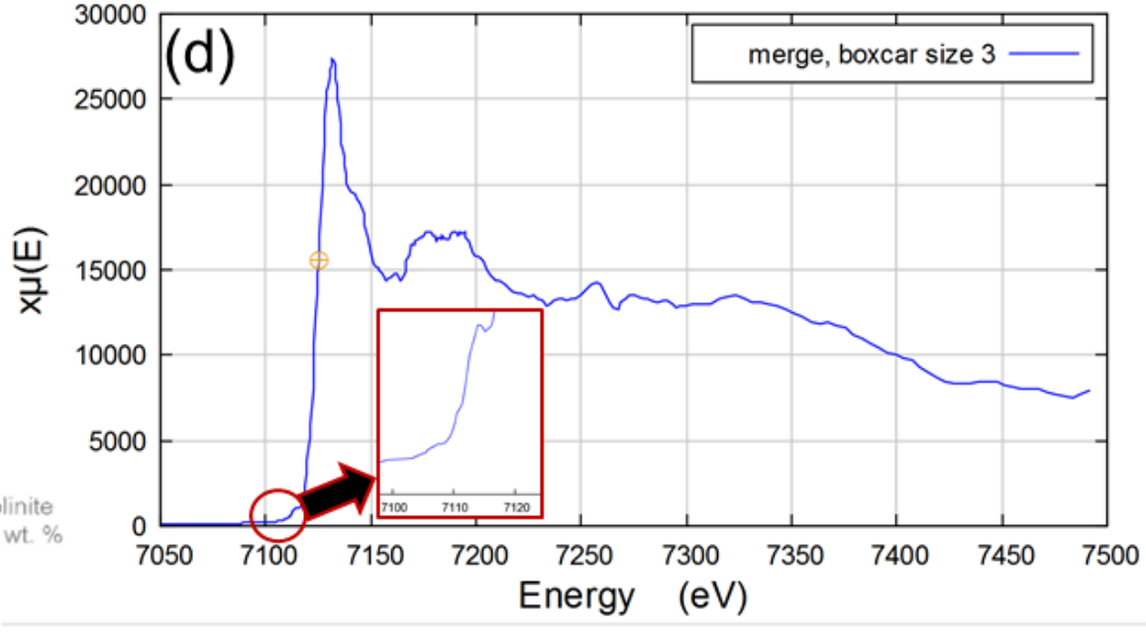
(d)
merge, boxcar size 3
xµ(E)
Energy (eV)
30000
25000
20000
15000
10000
5000
0
7050
7100
7150
7200
7250
7300
7350
7400
7450
7500
7100
7110
7120

Figure 4.

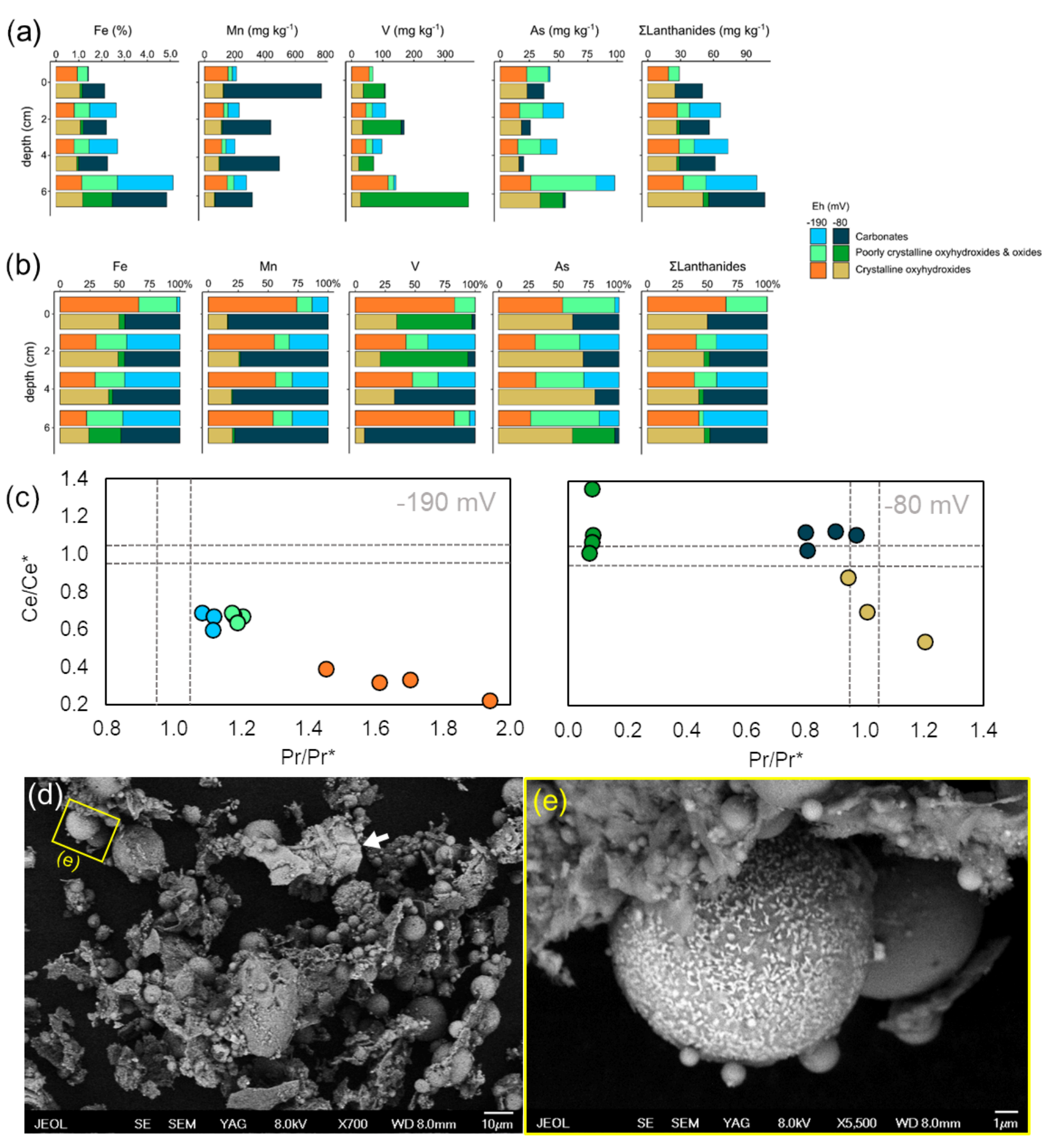
(a)
Fe (%)
Mn (mg kg-1)
V (mg kg-1)
As (mg kg-1)
ΣLanthanides (mg kg-1)
depth (cm)
Eh (mV)
-190 -80
Carbonates
Poorly crystalline oxyhydroxides & oxides
Crystalline oxyhydroxides
(b)
Fe
Mn
V
As
ΣLanthanides
depth (cm)
(c)
-190 mV
-80 mV
Ce/Ce*
Pr/Pr*
(d)
(e)
JEOL SE SEM YAG 8.0kV X700 WD 8.0mm 10μm
JEOL SE SEM YAG 8.0kV X5,500 WD 8.0mm 1μm

Figure 5.

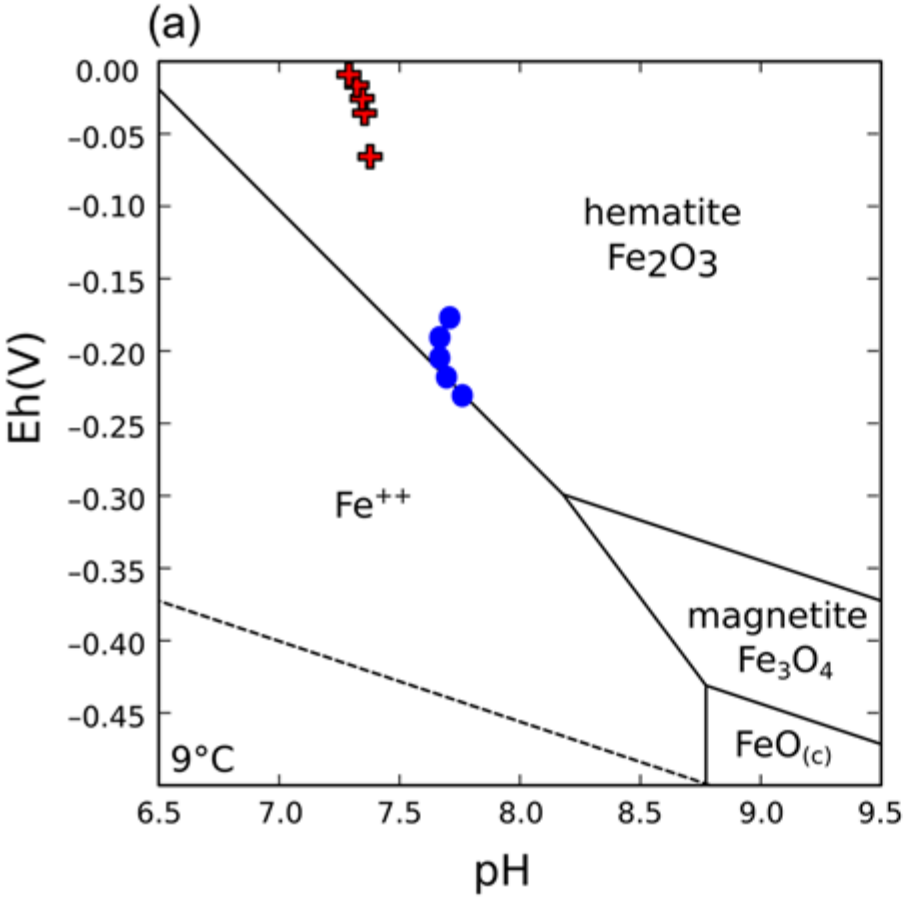
(a)
0.00
−0.05
−0.10
−0.15
−0.20
−0.25
−0.30
−0.35
−0.40
−0.45
Eh(V)
hematite
Fe2O3
Fe++
magnetite
Fe3O4
FeO(c)
9°C
6.5
7.0
7.5
8.0
8.5
9.0
9.5
pH

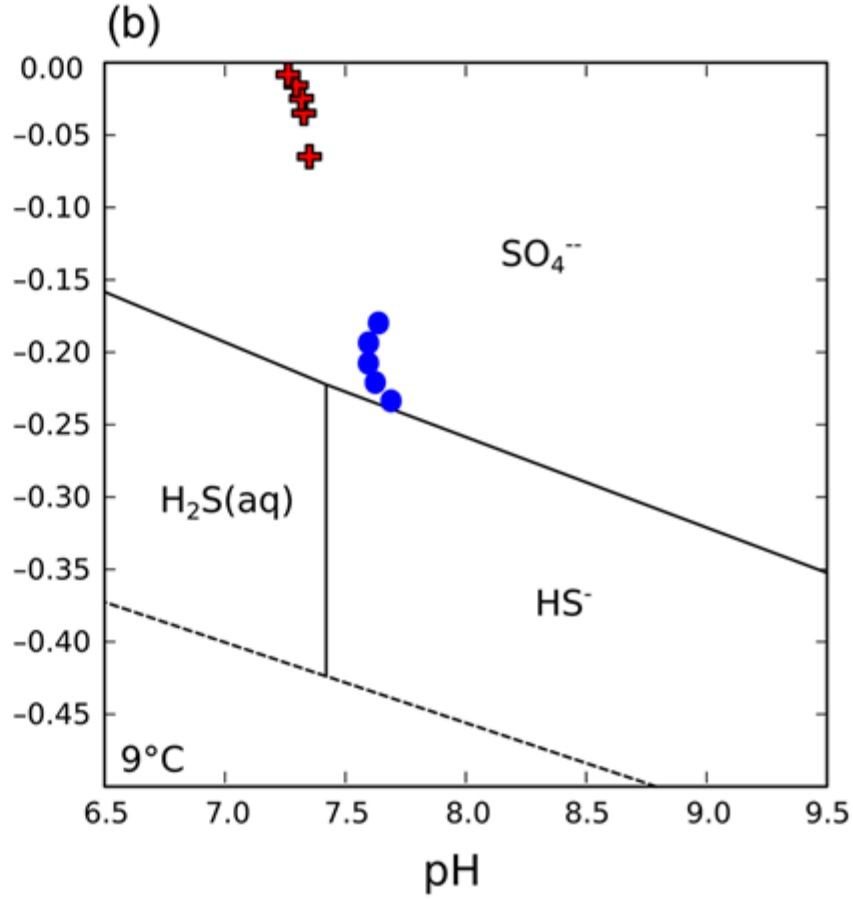
(b)
0.00
−0.05
−0.10
−0.15
−0.20
−0.25
−0.30
−0.35
−0.40
−0.45
SO4--
H2S(aq)
HS-
9°C
6.5
7.0
7.5
8.0
8.5
9.0
9.5
pH

Table 1. Dissolved concentrations of manganese (Mn^{2+}) and dissolved concentrations and stable isotope ratios of iron (Fe^{2+}), inorganic carbon (i.e., $\Sigma CO_2 = H_2CO_3 + HCO_3^- + CO_3^{2-}$) and sulfate ($SO_4^{2-}$) at the central deepest part of LM (47 to 55 m depth below the surface). The corresponding physicochemical parameters and dissolved trace metal contents pertaining the sampled bottom water column are shown in the Supplementary Material 1, Table SM1

Depth (m)	**Mn^{2+} (µM)**	**Fe^{2+} (µM)**	**δ^{56}Fe (‰)**	**DIC (mM)**	**$\delta^{13}C$ $(‰)_{VPDB}$**	**SO_4^{2-} (mM)**	**$\delta^{34}S$-SO_4^{2-} $(‰)_{VCDT}$**	**$\delta^{18}O$- SO_4^{2-} $(‰)_{VSMOW}$**
47	0.33 ± 0.01	0.07 ± 0.01	nd.	nd.	nd.	6.00 ± 0.80	+10.90 ± 0.10	nd.
48	0.42 ± 0.01	0.07 ± 0.01	nd.	1.90 ± 0.10	+0.20 ± 0.05	5.90 ± 0.80	+13.50 ± 0.07	+13.20 ± 0.20
48.5	19.92 ± 0.36	0.07 ± 0.01	nd.	3.50 ± 0.20	-0.10 ± 0.05	8.30 ± 0.80	+11.30 ± 0.03	+13.10 ± 0.05
49	20.11 ± 0.36	0.07 ± 0.01	-01.77 ± 0.03	7.50 ± 0.10	-2.10 ± 0.03	9.60 ± 1.60	+11.50 ± 0.10	+14.20 ± 0.10
50	30.57 ± 0.55	22.80 ± 0.40	-0.64 ± 0.08	5.90 ± 0.10	-2.70 ± 0.10	12.80 ± 1.60	+12.10 ± 0.10	+12.70 ± 0.40
52	14.62 ± 0.26	20.50 ± 2.30	-0.10 ± 0.05	9.80 ± 0.20	-2.50 ± 0.10	14.40 ± 0.70	+12.50 ± 0.10	+13.80 ± 0.20
54	13.72 ± 0.25	32.70 ± 6.50	+0.12 ± 0.05	9.00 ± 0.20	-3.90 ± 0.40	16.80 ± 0.70	+13.30 ± 0.10	+13.20 ± 1.10
55	11.08 ± 0.20	28.10 ± 5.60	+0.27 ± 0.10	nd.	nd.	16.00 ± 0.70	nd.	nd.

nd.: Not determined

Table 2. Concentrations of Al, Fe (wt%), and Mn, V, As, the sum of lanthanides, and redox sensitive Ce (mg kg^{-1}), along with Ce anomalies (Ce*) in LM's anoxic sediment cores from 0 to 8 cm depth. These concentrations were determined after sequential extraction and spectroscopic analysis of the extracts. Sediment samples were collected under varying Eh conditions in the overlying bottom water column, specifically from monimolimnion layers at -180 and -90 mV. TOC values, exhibiting minor variability, are further detailed in the footnote of this table.

Depth range (cm)	Fraction	Fe (wt. %)		Mn (mg kg^{-1})		V (mg kg^{-1})		As (mg kg^{-1})		ΣREE (mg kg^{-1})		Ce (mg kg^{-1})		Ce*	
		-190 mV	-80 mV	-190 mV	-80 mV	-190 mV	-80 mV	-190 mV	-80 mV	-190 mV	-80 mV	-190 mV	-80 mV	-190 mV	-80 mV
0-2	Carbonates	0.04	0.98	28.18	646.01	<L.Q	2.88	1.42	14.45	0.10	25.01	0.10	10.99	nd.	1.32
	Poorly crystalline oxyhydroxides	0.93	1.05	156.38	123.68	56.61	37.59	22.72	23.10	18.92	24.91	6.04	11.44	0.79	1.30
	Crystalline oxyhydroxides	0.45	0.10	26.95	4.63	11.70	67.84	18.50	<L.Q	9.87	<L.Q	1.15	<L.Q	0.45	nd.
2-4	Carbonates	1.17	1.02	74.46	321.63	43.14	10.10	17.64	7.71	28.26	27.14	9.01	11.81	0.79	1.29
	Poorly crystalline oxyhydroxides	0.79	1.07	126.43	112.12	46.36	35.26	16.58	18.17	27.00	26.51	8.81	12.92	0.77	1.92
	Crystalline oxyhydroxides	0.67	0.12	28.55	5.36	19.98	123.29	19.98	<L.Q	11.20	2.56	2.07	1.03	0.41	0.90
6-8	Carbonates	1.24	1.27	60.61	394.91	30.02	<L.Q	14.19	4.05	31.01	32.89	9.52	14.72	0.80	1.30
	Poorly crystalline oxyhydroxides	0.79	0.91	113.46	96.13	46.44	23.12	15.09	16.09	28.66	26.44	9.57	12.04	0.79	1.24
	Crystalline oxyhydroxides	0.67	0.07	28.18	4.48	20.69	47.48	19.34	<L.Q.	13.75	2.33	2.53	0.79	0.49	0.71

TOC values decrease with increasing depth, remaining within the analytical error for both sediment sampling campaigns. They range from 5.1 ± 0.2 (at the SWI) to 3.7 ± 0.4 (at a sediment pile depth of 6-8 cm). The TOC predominantly consists of refractory lignitic particles. The repeatability of the core analyses, expressed as the relative standard deviation, varies for different elements. For V, Mn, and Fe, the repeatability ranges from 4.4% to 9.0%; for As, it ranges from 8.3% to 10.6%; and for REE, it ranges from 1.5% to 10.8%; all percentages being relative to the reported values. <L.Q.: less than the quantification limit

Table 3. Saturation indices (log (IAP/K_{sp})) estimated for various minerals in theoretical equilibrium with LM's bottom water column at two distinct monimolimnial's redox potentials (i.e., -190 and -80 mV)

	Sat. Index*			Sat. Index *	
Mineral	-190 mV	-80 mV	Mineral	-190 mV	-80 mV
$Al(OH)_3$ (am)	0.786	0.328	Huntite	-0.205	0.597
Al_2O_3(s)	3.165	2.141	Hydroxyapatite	4.066	2.49
Anhydrite	-1.814	-1.823	Lepidocrocite	8.586	9.271
Aragonite	-0.564	-0.329	Mackinawite	-1.163	-0.363
Brucite	-3.561	-2.42	Magnesite	0.889	1.232
$Ca_3(PO_4)_2$ (beta)	-1.598	-2.972	Magnetite	24.919	27.777
$CaCO_3xH_2O$(s)	-1.747	-1.498	$MnCO_3$ (am)	-0.882	-0.041
Calcite	-0.408	-0.17	$MnHPO_4$(s)	1.006	0.113
Chalcedony	0.21	0.201	Na-Jarosite	2.433	1.814
Cristobalite	0.013	0.005	Pyrite	6.746	12.621
Diaspore	4.792	4.356	Quartz	0.686	0.685
Dolomite (disordered)	0.503	0.908	Rhodochrosite	-0.4	0.435
$Fe(OH)_2$ (c)	-2.44	-0.354	Sepiolite (A)	-0.069	2.672
$Fe_3(OH)_8$(s)	10.14	13.596	Siderite	-0.455	0.428
Ferrihydrite	5.772	6.169	SiO_2 (am)	-0.645	-0.667
FeS (ppt)	-1.921	-1.152	Spinel	-0.642	-0.568
Gibbsite (C)	3.905	3.464	Strengite	1.828	-0.429
Goethite	8.873	9.383	Struvite	-2.818	-3.508
Gypsum	-1.486	-1.471	Variscite	0.216	-2.867
Hematite	20.069	21.068	Vaterite	-1.019	-0.793
H-Jarosite	-4.352	-5.783	Vivianite	0.282	0.727

*Calculated by using the Visual Minteq 3.1 code with the following input values: temperature = 9.2/4.8 °C, pH = 7.7/8.2, ionic strength = 0.06/0.04 M, O_2 = 0.002/0.06 mM, Alkalinity (as $HCO3^-$) = 177/147 mg L^{-1}, DOC = 12 mg L^{-1}, DIC = 9.0 mM, Na^+ = 24.0/17.0 mM, K^+ = 0.31/0.27 mM, Ca^{2+} = 4.0/3.7 mM, Mg^{2+} = 445.0 mM, Si = 0.29/0.25 mM, Al^{3+} = 0.05 mM, Fe^{2+} = 0.028/0.117 mM, Fe^{3+} = 0.172/0.131 mM, Mn^{2+} = 0.011/0.040 mM, PO_4^{3-} = 0.02/0.001 mM, SO_4^{2-} = 16.0/20.0 mM, HS^- = 0.00025 mM, NO_3^- = 0.017/0.040 mM, and NH_4^+ = 0.127/0.142 mM for -190 mV and -80 mV, respectively.